Theoretical and experimental analysis of a partially textured thrust bearing with square dimples

V. G. Marian, M Kilian and W Scholz

Proceedings of the Institution of Mechanical Engineers, Part J: Journal of Engineering Tribology 2007 221: 771
DOI: 10.1243/13506501JET292

Theoretical and experimental analysis of a partially textured thrust bearing with square dimples

V G Marian[1*], **M Kilian**[2], and **W Scholz**[3]
[1]Laboratory of Machine Elements and Tribology, University Politehnica of Bucharest, Bucharest, Romania
[2]Institute for Engineering Design and Machine Elements, University of Kassel, Kassel, Germany
[3]Institute for Nanostructure Technologies and Analytics, University of Kassel, Kassel, Germany

The manuscript was received on 11 April 2007 and was accepted after revision for publication on 24 July 2007.

DOI: 10.1243/13506501JET292

Abstract: Surface texturing has proved to be very efficient in full and mixed lubrication, reducing the friction coefficient and the wear rate of mating surfaces. By partially texturing the inlet zone of a thrust washer pad load carrying capacity is generated in the system. In the present paper, a partially textured thrust bearing with square dimples is analysed theoretically using a thermo-hydrodynamic model. The equations are solved numerically by the finite-difference method. The bearing was realized by the photolithographic method and the theoretical results (fluid film thickness and friction torque) were compared with the experimental data obtained on the test rig. It is found that an optimal number of 12 sectors maximize the load carrying capacity of the bearing. The optimal textured fraction, which maximizes the load carrying capacity is 0.5 on the circumferential direction and 0.9–1 on the radial direction. A good correlation was found between the theoretical and experimental results for the two measured parameters (fluid film thickness and friction torque).

Keywords: hydrodynamic lubrication, thrust bearings, surface texturing, thermal effects in hydrodynamics

1 INTRODUCTION

Load carrying capacity is created in the fluid film of a couple having one textured surface even if the two mating surfaces are parallel, improving the tribological performance of the friction couple [**1**–**3**]. Surface texturing has proved to be very efficient in full and mixed lubrication, reducing the friction coefficient and the wear rate [**4**–**6**]. From the manufacturing point of view the most applied methods are laser texturing [**7**], photolithography [**5**, **8**], and abrasive jet machining [**9**]. Textured surfaces were introduced in a variety of applications from mechanical seals [**10**] to piston rings [**11**, **12**] and cylinder liners [**13**]. Load carrying capacity is also generated by a roughness effect at the entrance zone of a thrust washer [**14**]. This roughness effect could be generated by surface texturing [**15**–**18**]. The film thickness is larger at the entrance zone, creating an effect, which is similar to a converging wedge. The studies presented until recently describe bearings partially textured only in the circumferential direction and an isothermal model was used. The current study presents the effects of partial texturing both in the circumferential and in the radial direction of motion, introducing also a thermo-hydrodynamic modelling of the lubrication processes.

2 THEORETICAL ANALYSIS

The following main assumptions are considered: the lubricant is a Newtonian fluid with no slip at the boundary walls, the flow is considered laminar, the fluid viscosity varies with the temperature, the fluid does not exchange heat with the walls (adiabatic model), and all usual assumption for thin film lubrication are valid. The fluid manometric pressure is considered to be zero at the sector borders.

*Corresponding author: *Department of Machine Elements and Tribology, University Politehnica of Bucharest, Splaiul Independentei 313, Bucharest 060042, Romania. email: victormarian@omtr.pub.ro*

The dimples are considered to have a square form and the bearing was modelled in cylindrical coordinates. The term 'square dimple' was employed in order to simplify the language. The real form of the dimple is parallelopiped having a square as upper area.

2.1 Governing equations

2.1.1 Reynolds and energy equation

The model is presented in cylindrical coordinates (Fig. 1). Based on the adiabatic assumption mentioned above, it is considered that the temperature and hence the viscosity does not vary over the film thickness. The Couette approximation is used, i.e. the effect of the pressure gradient on the rate of shear stress is neglected. The two equations to be considered are

$$\eta \frac{\partial^2 u}{\partial y^2} = \frac{1}{r}\left(\frac{\partial p}{\partial \theta}\right) \tag{1}$$

$$\eta \frac{\partial^2 v}{\partial y^2} = \frac{\partial p}{\partial r} \tag{2}$$

with the boundary conditions

$$u = r\omega, \quad v = 0 \quad \text{for} \quad y = 0$$
$$u = 0, \quad v = 0 \quad \text{for} \quad y = h$$

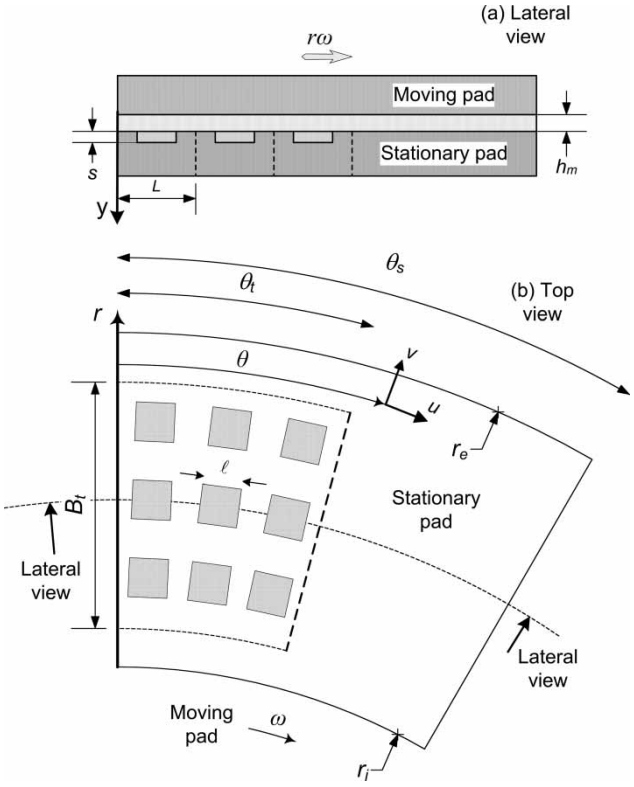

Fig. 1 Schematic of a partially textured bearing pad

Integrating equation (1) yields for the velocity

$$u = \frac{\omega r}{h}(h - y) - \frac{y(h - y)}{2\eta r}\frac{\partial p}{\partial \theta} \tag{3}$$

The fluid viscosity is considered to be

$$\eta = \eta_i e^{-\beta(T - T_i)} \tag{4}$$

For determining the temperature field over the bearing sector the effect of the pressure gradient on the rate of shear stress was neglected (Couette approximation). The great merit of this approach is that the energy equation is uncoupled from the Reynolds equation, greatly simplifying both the computational labour and the resulting solutions [**19**]. Due to the large amount of discretization nodes in the numerical solution, a more complex model would dramatically increase the computing time. The adiabatic heat convection equation due to the energy dissipated by viscous shear is given by

$$\rho c u \frac{\partial T}{\partial x} = \eta \left(\frac{\partial u}{\partial y}\right)^2 \tag{5}$$

Using equation (3) for the velocity and its derivative, the above expression becomes

$$\frac{\partial T}{\partial \theta} = 2\omega \frac{\eta}{\rho \cdot c}\left(\frac{r}{h}\right)^2 \tag{6}$$

Inserting the equation (4) in equation (6) and the resulting expression integrated

$$e^{\beta(T - T_i)} = 1 + E\bar{r}^2 \int_0^{\theta} \frac{d\theta}{\bar{h}^2} \tag{7}$$

where

$$E = \frac{2\eta_i \omega \beta}{\rho \cdot c}\left(\frac{r_i}{h_m}\right)^2 \tag{8}$$

Using the equation (7) and (4), the lubricant viscosity and temperature can be obtained

$$\bar{\eta} = \frac{1}{1 + E\bar{r}^2 \int_0^{\theta} (d\theta / \bar{h}^2)} \tag{9}$$

$$T = \frac{\ln(1/\bar{\eta})}{\beta} + T_i \tag{10}$$

Using the equation (1) and (2) and the continuity equation, the Reynolds equation can be obtained

$$\frac{\partial}{\partial \bar{r}}\left(\frac{\bar{r}}{\bar{\eta}}\frac{\partial \bar{p}}{\partial \bar{r}}\right) + \frac{1}{\bar{r}}\frac{\partial}{\partial \theta}\left(\frac{1}{\bar{\eta}}\frac{\partial \bar{p}}{\partial \theta}\right) = 0 \tag{11}$$

2.1.2 *Load carrying capacity*

The total thrust force of the bearing is

$$\bar{F} = \frac{Fh_m^2}{\eta_i \omega r_i^4} = n_s r \int_1^{\bar{r}_e} \int_0^{\theta_s} \bar{p} \cdot \bar{r} \cdot d\theta \cdot d\bar{r} \tag{12}$$

2.1.3 *Friction coefficient and friction torque*

In order to compare the theoretical results with the experimental data, the friction torque at the textured surface (stationary surface) was calculated. The shear tension at the textured surface is

$$\tau = -\frac{h}{2}\frac{dp}{dx} + \eta \frac{r\omega}{h} \tag{13}$$

In dimensionless coordinates the shear tension is

$$\bar{\tau} = \frac{\tau h_m}{\eta_i \omega r_i^4} = \frac{\bar{\eta}\bar{r}}{\bar{h}} - \frac{\bar{h}}{2\bar{r}}\frac{d\bar{p}}{d\theta} \tag{14}$$

The friction force is

$$\bar{F}_f = \frac{F_f h_m}{\eta_i \omega r_i^3} = n_s \int_{\text{pad surface}} \int \overline{\tau r}\, d\theta\, d\bar{r} \tag{15}$$

The friction coefficient is

$$\bar{\mu} = \frac{\bar{F}_f}{\bar{F}} = \frac{\mu r_i}{h_m} \tag{16}$$

The friction torque of the bearing is

$$\bar{M}_f = \frac{M_f h_m}{\eta_i \omega r_i^4} = n_s \int_{\text{pad surface}} \int \overline{\tau r}^2\, d\theta\, d\bar{r} \tag{17}$$

2.1.4 *Numerical method of solution*

Equations (9) to (11) were solved numerically using the finite difference method. The expression $\int_0^{\theta} d\theta/\bar{h}^2$ was calculated by numerical integration (the values of the film height being discontinuous). The system of equations obtained was solved using the biconjugate gradient stabilized method with incomplete lower-upper (ILU) preconditioner. Equations (9) to (10) were solved obtaining the temperature and the viscosity field, then the viscosity field was used in equation (11) to obtain the pressure distribution. The flow conservation was applied on the discontinuity points (Fig. 2). A mesh size of 32 intervals for one cell was utilized. Refining the mesh leads to an insignificant improvement of the results and to a major increase in computing time.

The temperature distribution over the bearing pad is presented in Fig. 3. The bearing presents the following characteristics: $r_i = 28.5$ mm, $r_e = 45$ mm, $n_s = 12$, $\ell_c = 2$ mm, $h_m = 10\,\mu$m, $s = 9\,\mu$m, $n = 500$ rpm, $N_1 = N_2 = 22$, $\rho_t = 0.25$, $\alpha_1 = 0.5$, $\alpha_2 = 0.5$, $T_i = 45\,^\circ$C, $\eta_i = 0.0220$ Pa·s, $\beta = 0.0367\,K^{-1}$, $\rho = 848\,kg/m^3$, $c = 1.95\,kJ/(kg\,^\circ K)$. It can be remarked that the maximal temperature is situated on the upper right corner because the distance between the inlet and the outlet of the fluid is maximal on the outer margin of the bearing.

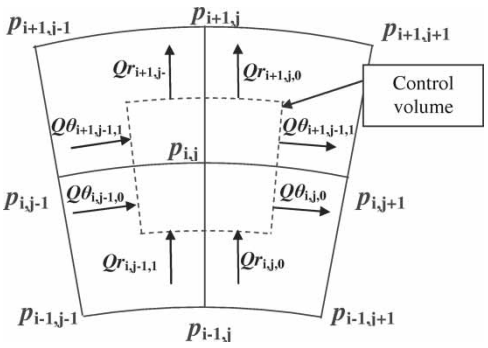

Fig. 2 Flow balance at discontinuity point

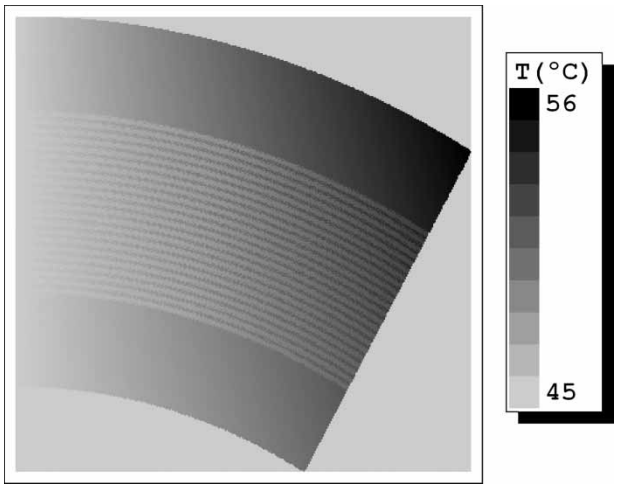

Fig. 3 Temperature distribution of a bearing pad

The pressure distribution of a bearing pad is presented in Fig. 4. One can remark that the shape

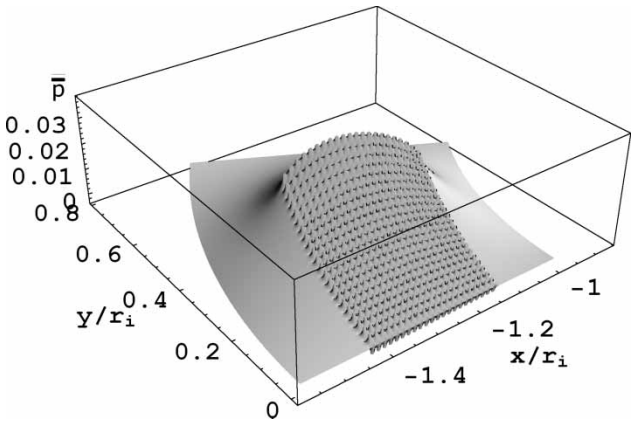

Fig. 4 Fluid pressure distribution of a bearing pad

of the pressure distribution is similar to the pressure distribution of a stepped bearing. The pressure distribution obtained on the first column of dimples is less than zero. As a model including cavitation would increase the computing time, a smaller model including a simplified cavitation model (pressures smaller than zero are forced to zero inside each iteration) was used. The pressure obtained is higher than the pressure obtained without cavitation model, but the difference is extremely small. The mean pressure would be practically the same using the model with cavitation compared with the model without cavitation.

Determining the optimal number of pads is essential in finding the optimal configuration for the bearing, which maximizes the load carrying capacity. One can notice from Fig. 5 that the number of pads that produces a maximal load carrying capacity is 12.

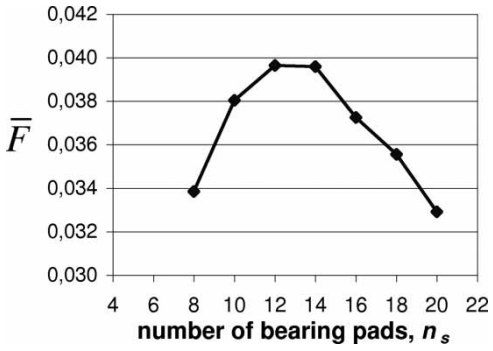

Fig. 5 Variation of load carrying capacity versus number of bearing pads

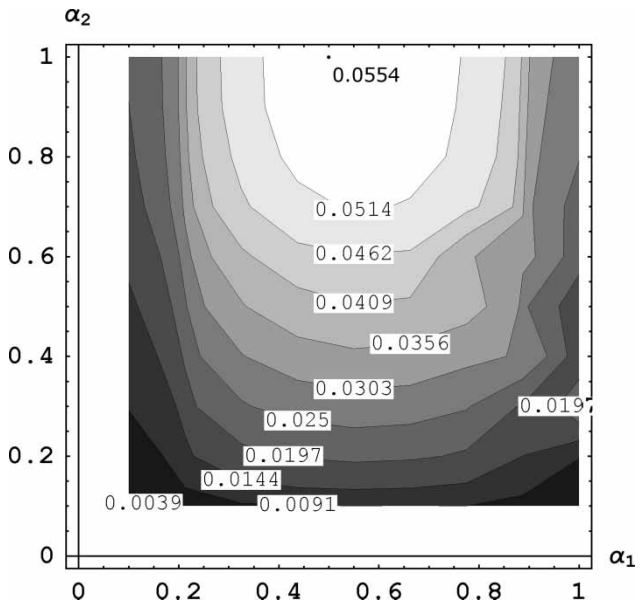

Fig. 6 Variation of dimensionless load carrying capacity versus textured fraction

The following parameters are used in this case:

$$\bar{s} = 1; r_e/r_i = 45/28.5; \rho_t = 0.25; N_2 = 28;$$
$$\alpha_1 = 0.7; \alpha_2 = 0.7.$$

The variation of the dimensionless load carrying capacity with the textured fraction is presented in Fig. 6. All the others parameters are the same as those for the bearing calculated and presented in Fig. 3. The maximal load carrying capacity is obtained for $\alpha_1 = 0.5$ and $\alpha_2 = 0.9-1$.

The optimal values obtained above are used in the fabrication of the sample bearing presented below.

3 EXPERIMENTAL ANALYSIS

The experimental setup consisted in choosing the best configuration for the bearing, the comparative analysis of the technologies to be used to realize the textured surfaces in conformity with the dimensional requirements from the theoretical study, the fabrication of the textured bearing samples, their dimensional evaluation and finally the testing of the bearing samples on the test rig.

3.1 Micromechanical fabrication of the partially textured bearing

The square dimples were realized by the photolithographic method. A flat axial roller bearing ring, 7 mm thick was used as substrate for the process. The ring has an inner diameter of 57 mm and an outer diameter of 90 mm. The main advantage of the ring consists of his extremely flat surface (maximal waviness = 1 μm). The UV lithography process begins by casting a layer of SU8, a viscous epoxy based photo polymer, onto the substrate. The substrate is then spun on a spin coater for a desired time and spin speed to deposit a uniform layer of SU-8 on the substrate surface. The substrate is then placed on a level hot plate and baked for a desired time and temperature. It is then exposed to UV light in the presence of a photomask (having rectangular patterns) to transfer the desired pattern onto the substrate and baked again and developed in an SU-8 developer solution to yield an array of square structures uncovered by the SU8 photoresist. Finally the substrate was etched electrolytically, obtaining in the end the desired textured surface. A number of 12 sectors were etched on each bearing in order to obtain maximal load carrying capacity in accordance with the theoretical results obtained in the previous section. After the bearings were etched, a number of 12 channels for the oil supply were milled onto the substrate (Fig. 7).

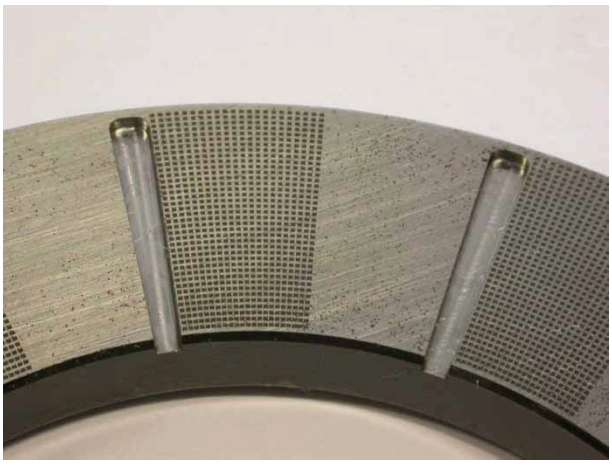

Fig. 7 Photograph of a bearing pad

3.2 Dimensional characteristics of the textured bearing

After the fabrication steps presented in the preceding section, one bearing sample was fabricated with the characteristics presented in Table 1.

A sample of dimples measured using a three-dimensional measuring laser machine in presented in Fig. 8.

3.3 Test rig

The test rig is schematically presented in Fig. 9. The electric motor (1) rotates the untextured ring (13). The load created by the hydraulic cylinder (3) is measured by the load cell (7). The oil is supplied to the system by the oil circuit (6). The system is not immersed in an oil bath, the necessary oil being supplied through the oil nozzle (15). The friction torque is measured by the load cell (9), which prevents the rotation of the textured ring (10), fixed on the roller bearing (8).

The oil film thickness is measured by the proximity probe (2). The temperature on two points of the test rig was measured by the thermocouples (12). The contact sensor (5) detects if the bearing is in full-film lubrication or mixed lubrication.

4 RESULTS

The variation of fluid film thickness function of rotation speed is presented in Fig. 10 for 100, respectively, 200 N axial load.

The textured bearing has the following characteristics (ring EROZ 01 from Table 1): $r_i = 28.5$ mm, $r_e = 45$ mm, $\ell = 200\,\mu$m, $n_s = 12$, $s = 9\,\mu$m, $N_1 = 22$, $N_2 = 38$, $\rho_t = 0.25$, $\alpha_1 = 0.5$, $\alpha_2 = 0.9$, $T_i = 45°$C, the lubricant having $\eta_i = 0.0220$ Pa·s, $\beta = 0.0367\,\text{K}^{-1}$, $\rho = 848\,\text{kg/m}^3$, $c = 1.95\,\text{kJ/(kg}\,°\text{K)}$.

It can be remarked that the theoretical model presents higher film thicknesses than the experimental data. An explanation of this phenomenon could be that the lubrication is not realized by immersion, thus leading to insufficient lubricant in some regions of the bearing. However, the differences between the experimental and theoretical data are relatively small.

The variation of the friction torque function of rotation speed for the same ring is presented in Fig. 11. In order not to cumulate the difference between the experimental and the theoretical values of the

Table 1 Bearing parameters

Model	Dimple side ℓ (μm)	Textured fraction on circumferential direction α_1	Textured fraction on radial direction α_2	Dimple depth s (μm)
EROZ 01	200	50%	90%	9

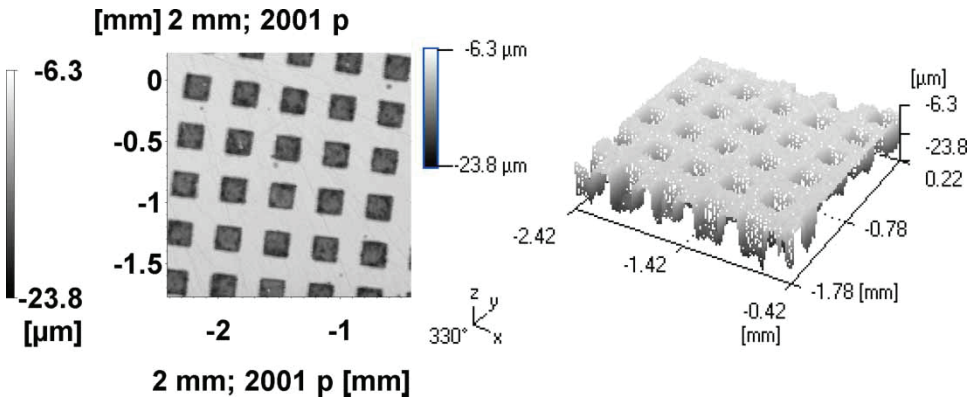

Fig. 8 Three-dimensional measurement of the dimples topography

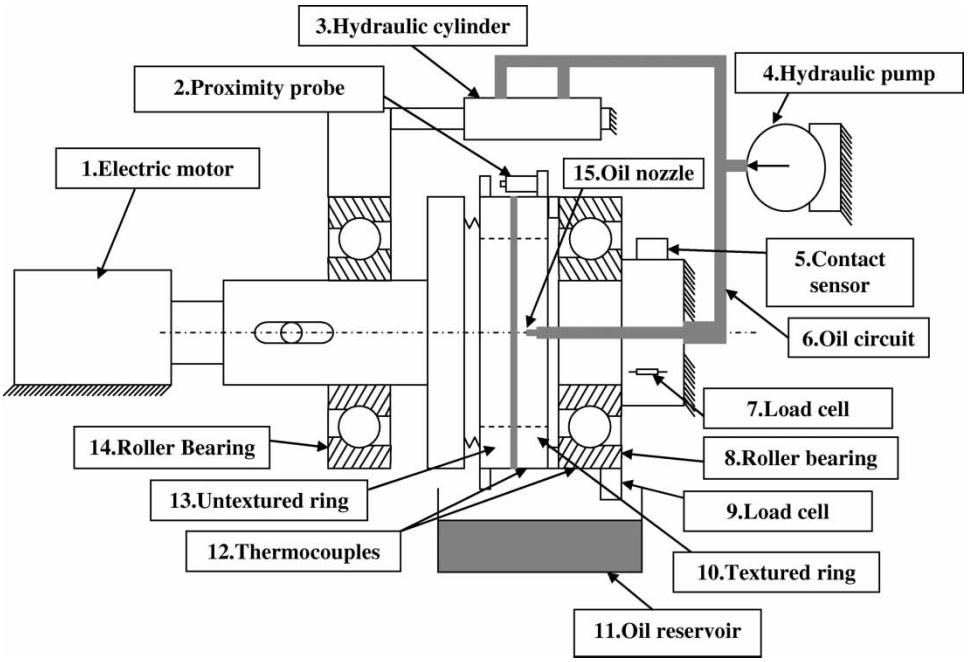

Fig. 9 A schematic description of the test rig

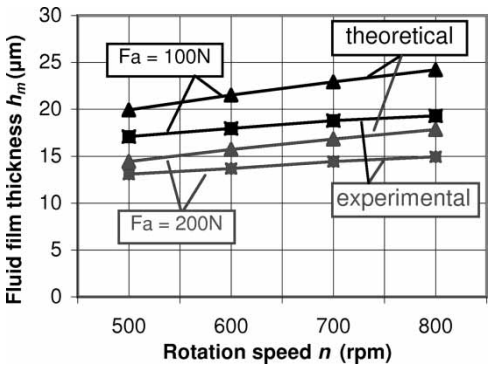

Fig. 10 Variation of fluid film thickness versus rotation speed

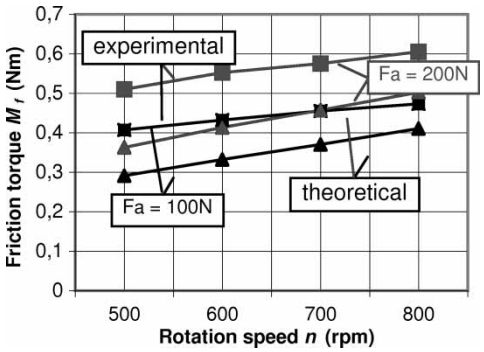

Fig. 11 Variation of friction torque versus rotation speed

film thickness, the experimental values of the film thickness were used for computing the friction torque. It can be remarked that the measured friction torque is higher than the theoretical values. The difference could be explained from the measurement errors due to induced vibrations, the measured torque presenting oscillations over one rotation (the values experimental values presented in Fig. 11 are mean values of the measured values over time).

An untextured ring was also tested in order to observe the influence of the dimples on the friction coefficient. The friction torque obtained for $F_a = 100$ N is 0.544 Nm for $n = 200$ rpm and 0.665 Nm for $n = 400$ rpm. For higher rotation speeds the values of the friction torque were above the maximal value, which could be measured by the load cell. For the untextured ring, no load carrying capacity is theoretically expected. In this case, the measured friction torque certainly results of mixed lubrication conditions and it is not a surprise to obtain largely higher values than for the pad with dimples. In conclusion, the textured bearing presents lower friction coefficients than the untextured bearing.

5 CONCLUSIONS

It can be concluded that wet etching is a reliable method for producing textured bearing samples. Using the assumptions of an adiabatic model (no heat exchange between the fluid film and the bearing walls), the following optimal parameters were found for the present textured bearing:

(a) an optimal number of 12 sectors maximize the load carrying capacity;

(b) the optimal textured fraction that maximizes the load carrying capacity is 0.5 on the circumferential direction and 0.9–1 on the radial direction.

A good correlation is found between the theoretical and experimental results. The textured bearing presents lower friction coefficients than the untextured specimen.

ACKNOWLEDGEMENTS

Financial support for the work described in the current paper was provided by the German Academic Exchange Service and the Romanian National Council for Academic Scientific Research (CNCSIS) under Grants No. 464/2006 and 1418/2005.

The authors express their gratitude to Mr Thomas Smetana of INA Schaeffler for providing the bearing specimens.

REFERENCES

1 **Anno, J. N., Walowit, J. A.,** and **Allen, C. M.** Microasperity lubrication. In ASME Annual Meeting, 67-WA/Lub-1, 1967.
2 **Hamilton, D. B., Walowit, J. A.,** and **Allen, C. M.** A theory of lubrication by micro-irregularities. In ASME-ASLE Lubrication Conference, 65-Lub-11, 1965.
3 **Sahlin, F., Glavatskih, S., Torbjörn, A.,** and **Larsson, R.** Two-dimensional CFD-analysis of micro-patterned surfaces in hydrodynamic lubrication. *J. Tribol.*, 2005, **127**(1), 96–102.
4 **Kovalchenko, A., Ajayi, O., Erdemir, A., Fenske, G.,** and **Etsion, I.** The effect of laser surface texturing on transitions in lubrication regimes during unidirectional sliding contact. *Tribol. Int.*, 2005, **38**, 219–225.
5 **Pettersson, U.** and **Jacobson, S.** Influence of surface texture on boundary lubricated sliding contacts. *Tribol. Int.*, 2003, **36**, 857–864.
6 **Wang, X., Kato, K., Adachi, K.,** and **Aizawa, K.** Loads carrying capacity map for the surface texture design of SiC thrust bearing sliding in water. *Tribol. Int.*, 2003, **36**, 189–197.
7 **Haefke, H., Cerbig, Y., Gabriel, D.,** and **Romano, V.** Microtexturing of functional surfaces for improving their tribological performance. In Proceedings of International Tribology Conference, Nagasaki, 2000, pp. 217–221.
8 **Siripuram, R. B.** and **Stephens, L. S.** Efect of deterministic asperity geometry on hydrodynamic lubrication. *J. Tribol.*, 2004, **126**(3), 527–534.
9 **Wakuda, M., Yamauki, Y., Kanzaki, S.,** and **Yasuda, Y.** Effect of surface texturing on surface reduction between ceramic and steel materials under lubricated sliding contact. *Wear*, 2003, **254**, 356–363.
10 **Etsion, I.** and **Halperin, G.** A laser surface textured hydrostatic mechanical seal. *Tribol. Trans.*, 2002, **45**(3), 430–434.
11 **Kligerman, Y., Etsion, I.,** and **Shinkarenko, A.** Improving tribological performance of piston rings by partial surface texturing. *J. Tribol.*, 2005, **127**(3), 632–638.
12 **Ryk, G., Kligerman, Y., Etsion, I.,** and **Shinkarenko, A.** Experimental investigation of partial laser surface texturing for piston ring friction reduction. *Tribol. Trans.*, 2005, **48**, 583–588.
13 **Golloch, R., Merker, G. P., Kessen, U.,** and **Brinkmann, S.** Benefits of laser-structured cylinder liners for internal combustion engines. In 14th International Colloquium Tribology, Esslingen, Germany, 2004, vol. 1, pp. 321–328.
14 **Tonder, K.** A new class of bearings based on roughness effects. In STLE/ASME Tribology Conference, Orlando, FL, USA, 1999.
15 **Brizmer, V., Kligerman, Y.,** and **Etsion, I.** A laser surface textured parallel thrust bearing. *Tribol. Trans.*, 2003, **46**(3), 397–403.
16 **Etsion, I., Halperin, G., Brizmer, V.,** and **Kligerman, Y.** Experimental investigation of laser surface textured parallel thrust bearings. *Tribol. Lett.*, 2004, **17**(2), 295–300.
17 **Pascovici, M. D., Marian, V. G.,** and **Gaman, D.** Analytical and numerical approach of load carrying capacity for partially textured slider. In International Nanotribology Conference on Nano Sikkim II : Friction and Biotribology, Peeling, Sikkim, India, 2004.
18 **Wang, X., Kato, K., Adachi, K.,** and **Aizawa, K.** Running-in effect on the load-carrying capacity of a water-lubricated SiC thrust bearing. *Proc. IMechE, Part J: J. Engineering Tribology*, 2005, **219**(K2), 117–124.
19 **Pinkus, O.** and **Lund, J. W.** Centrifugal effects in thrust bearings and seals under laminar conditions, *J. Lubr. Technol.*, 1981, **103**(1), 126–136.

APPENDIX

Notation

B_t	textured width of a bearing pad
c	specific heat
E	adiabatic number, $\frac{2\eta_i\omega\beta}{g\rho c}\left(\frac{r_i}{h_m}\right)^2$
F	load carrying capacity
$\bar{F}$	dimensionless load carrying capacity, $\frac{Fh_m^2}{\eta_i\omega r_i^4}$
F_a	axial force
F_f	friction force
$\bar{F}_f$	dimensionless friction force, $\frac{F_f h_m}{\eta_i\omega r_i^3}$
g	gravity force
h	film thickness
h_m	minimal film thickness
$\bar{h}$	dimensionless film thickness, $\frac{h}{h_m}$
ℓ	dimple side dimension
ℓ_c	width of bearing oil supply channels at mean radius
L	cell side dimension
M_f	friction torque
n	rotation speed of runner
n_s	number of bearing pads

N_1	number of dimples on one pad on circumferential direction
N_2	number of dimples on one pad on radial direction
p	local pressure
$\bar{p}$	dimensionless pressure, $\frac{p \cdot h_m^2}{\eta_i \cdot \omega \cdot r_i^2}$
r	radial coordinate
r_e	outer radius of bearing
r_i	inner radius of bearing
$\bar{r}$	radial dimensionless coordinate $\frac{r}{r_i}$
$\bar{r}_e$	outer dimensionless radius of bearing, $\frac{r_e}{r_i}$
s	dimple depth
$\bar{s}$	dimensionless dimple depth, $\frac{s}{h_m}$
T	temperature
T_i	inlet oil temperature
u	velocity in the θ direction
v	velocity in the r direction
α_1	textured fraction on circumferential direction θ_t/θ_s
α_2	textured fraction on radial direction, $B_t/(r_e - r_i)$
β	viscosity–temperature coefficient
η	fluid dynamic viscosity
η_i	fluid dynamic viscosity at the inlet temperature T_i
$\bar{\eta}$	dimensionless dynamic viscosity, $\frac{\eta}{\eta_i}$
θ	angular coordinate
θ_s	angular span of a bearing pad
θ_t	angular span of the textured zone of a bearing pad
ρ	oil density
ρ_t	area density of dimples, (total area of the dimples)/(total area of the textured surface)
τ	shear stress
$\bar{\tau}$	dimensionless shear stress
ω	angular velocity of runner